Volume 22
Number 34
14 September 2020
Pages 18725–19378

PCCP

Physical Chemistry Chemical Physics

rsc.li/pccp

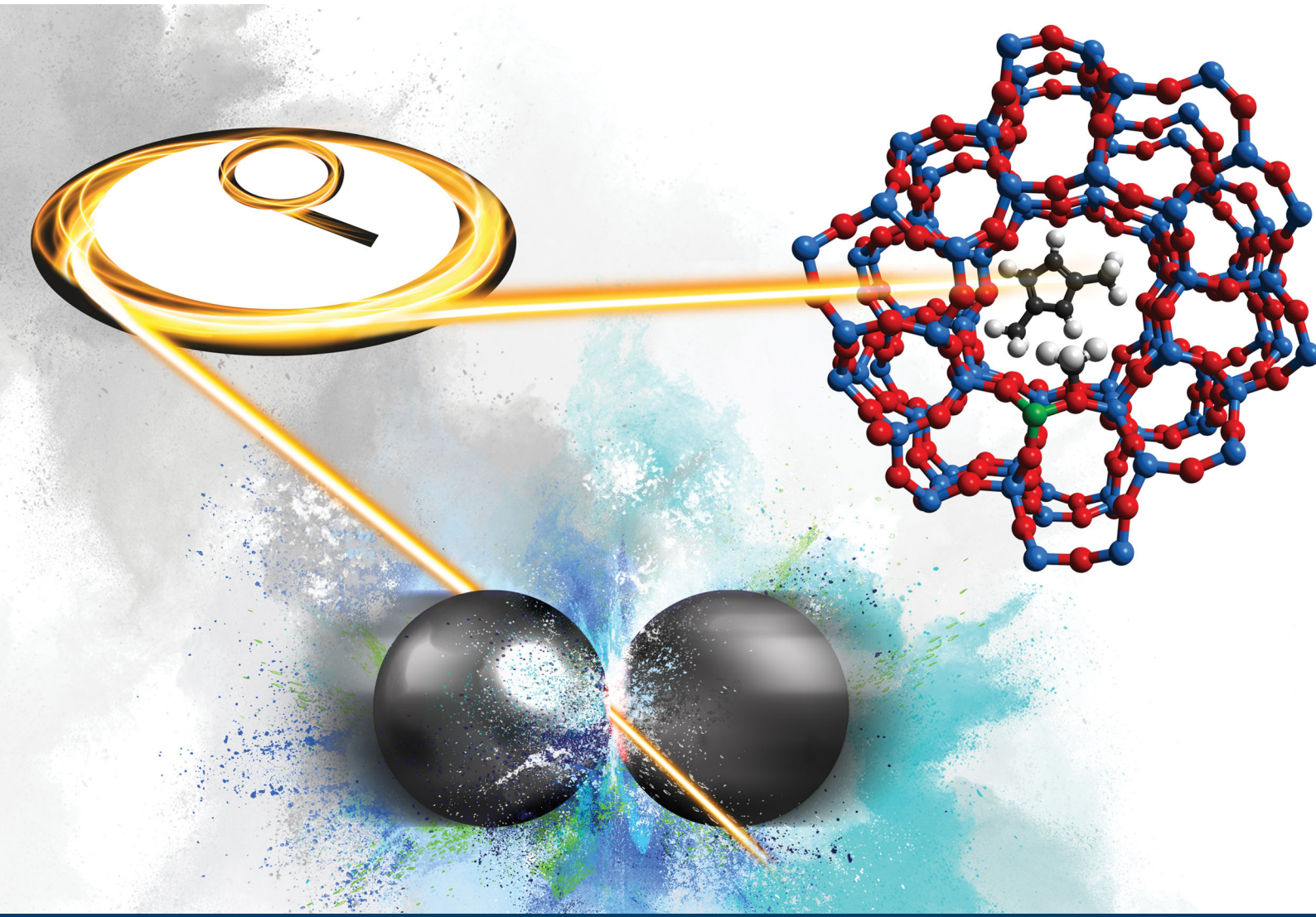

Themed issue: Synchrotron Radiation Techniques in Catalytic Science

ISSN 1463-9076

PAPERS

ROYAL SOCIETY OF CHEMISTRY

PCCP

ROYAL SOCIETY OF CHEMISTRY

PAPER

View Article Online
View Journal | View Issue

Check for updates

Cite this: *Phys. Chem. Chem. Phys.*, 2020, **22**, 18774

The electronic structure, surface properties, and *in situ* N_2O decomposition of mechanochemically synthesised $LaMnO_3$†

Rachel H. Blackmore,[ab] Maria Elena Rivas,[c] George F. Tierney,[ab] Khaled M. H. Mohammed,[bd] Donato Decarolis,[ae] Shusaku Hayama,[f] Federica Venturini,[f] Georg Held,[f] Rosa Arrigo,[fg] Monica Amboage,[f] Pip Hellier,[ae] Evan Lynch,[ab] Mahrez Amri,[c] Marianna Casavola,[b] Tugce Eralp Erden,[c] Paul Collier[c] and Peter P. Wells *[abf]

The use of mechanochemistry to prepare catalytic materials is of significant interest; it offers an environmentally beneficial, solvent-free, route and produces highly complex structures of mixed amorphous and crystalline phases. This study reports on the effect of milling atmosphere, either air or argon, on mechanochemically prepared $LaMnO_3$ and the catalytic performance towards N_2O decomposition (deN_2O). In this work, high energy resolution fluorescence detection (HERFD), X-ray absorption near edge structure (XANES), X-ray emission, and X-ray photoelectron spectroscopy (XPS) have been used to probe the electronic structural properties of the mechanochemically prepared materials. Moreover, *in situ* studies using near ambient pressure (NAP)-XPS, to follow the materials during catalysis, and high pressure energy dispersive EXAFS studies, to mimic the preparation conditions, have also been performed. The studies show that there are clear differences between the air and argon milled samples, with the most pronounced changes observed using NAP-XPS. The XPS results find increased levels of active adsorbed oxygen species, linked to the presence of surface oxide vacancies, for the sample prepared in argon. Furthermore, the argon milled $LaMnO_3$ shows improved catalytic activity towards deN_2O at lower temperatures compared to the air milled and sol–gel synthesised $LaMnO_3$. Assessing this improved catalytic behaviour during deN_2O of argon milled $LaMnO_3$ by *in situ* NAP-XPS suggests increased interaction of N_2O at room temperature within the O 1s region. This study further demonstrates the complexity of mechanochemically prepared materials and through careful choice of characterisation methods how their properties can be understood.

Received 12th February 2020,
Accepted 7th April 2020

DOI: 10.1039/d0cp00793e

rsc.li/pccp

Open Access Article. Published on 30 Qasa Dirri 2020. Downloaded on 22/04/2026 6:39:19 AM.
This article is licensed under a Creative Commons Attribution 3.0 Unported Licence.

1. Introduction

Developing catalytic processes that are both economically viable and sustainable represents a significant challenge. To meet this ambition, the development of new technologies can no longer rely on iterative trial and error approaches and must instead be design-led using sophisticated characterisation methods.[1] Synchrotron techniques, such as X-ray absorption spectroscopy (XAS), have multiple benefits, which aid the in-depth understanding of chemically important yet complex systems.[2–4]

Previously, we have reported the advantages of XAS for studying the preparation of metal oxides prepared through mechanochemistry; this solvent-free synthesis route produces less waste than traditional methods and prepares materials with enhanced catalytic properties.[5] Our recent study focussed on the mechanochemical synthesis of $LaMnO_3$ from its single oxide precursors. During this process there was a significant amount of amorphous material produced at different stages of milling. Traditional characterisation methods, such as X-ray diffraction (XRD), provided an incomplete understanding of the underlying chemistry. Using XAS, which provides structural insights on all length scales, allowed us to learn more about the principal chemical

[a] *UK Catalysis Hub, Research Complex at Harwell, Rutherford Appleton Laboratories, Harwell Science & Innovation Campus, Didcot, Oxfordshire, OX11 0FA, UK*
[b] *School of Chemistry, University of Southampton, Southampton, SO17 1BJ, UK. E-mail: P.P.Wells@soton.ac.uk*
[c] *Johnson Matthey Technology Centre, Blounts Court Road, Sonning Common, Reading, RG4 9NH, UK*
[d] *Department of Chemistry, Faculty of Science, Sohag University, Sohag, P. O. Box 82524, Egypt*
[e] *School of Chemistry, Cardiff University, Main Building, Park Place, Cardiff, CF10 3AT, UK*
[f] *Diamond Light Source Ltd., Harwell Science & Innovation Campus, Didcot, Oxfordshire, OX11 0DE, UK*
[g] *School of Science, Engineering and Environment, University of Salford, Manchester M5 4WT, UK*

† Electronic supplementary information (ESI) available. See DOI: 10.1039/d0cp00793e

This journal is © the Owner Societies 2020

Open Access Article. Published on 30 Qasa Dirri 2020. Downloaded on 22/04/2026 6:39:19 AM.
This article is licensed under a Creative Commons Attribution 3.0 Unported Licence.

steps within the milling process. Furthermore, these studies also increased the understanding of how these materials promote the catalytic decomposition of the environmental pollutant N_2O (deN_2O).

However, even after performing conventional XAS at the Mn K-edge information such as the local charge density and electronic configuration still eluded us. In this work we discuss the use of further advanced characterisation techniques, such as high energy resolution fluorescence detection (HERFD) to improve the XANES spectral resolution,[6,7] and X-ray emission spectroscopy (XES) to attain information on electronic structure and oxidation state.[8,9] Furthermore, we endeavoured to mimic the environmental conditions experienced during planetary ball milling by performing an *in situ* XAS study at high pressure in a diamond anvil cell (DAC). This was performed in conjunction with *in situ* vibrational ball milling by XRD. These new structural insights have then been coupled with *in situ* near ambient pressure X-ray photoelectron spectroscopy (NAP-XPS) to further understand how ball milled materials have improved catalytic activity at lower temperatures during deN_2O.

By combining these local structural and electronic techniques, along with surface sensitive characterisation, it can be a powerful tool for understanding how structural properties, induced by the syntheitic route, can affect catalysis. Herein, we report an in-depth analysis during the mechanochemically synthesised $LaMnO_3$ by XES and HERFD, not previously reported. Furthermore, we can now link these structural properties of the final material to the enhancement of catalytic activity for the *in situ* deN_2O combined with NAP-XPS.

2. Experimental

a. $LaMnO_3$ sample preparation

High energy planetary ball milling was performed at room temperature in a 4-station Fritsch Pulverisette 5 Planetary Ball Mill. ZrO_2 vessels were prepared with precursors Mn_2O_3 and La_2O_3 at the correct proportions to synthesise stoichiometric $LaMnO_3$, along with 5 mm ZrO_2 spheres at a sphere : powder ratio of 10 : 1. Milling was then conducted up to 4 hours at 400 rpm in sessions of 20 min, in both atmospheric and inert environments. For the sol–gel synthesis stoichiometric amounts of $Mn(NO_3)_2{\cdot}4H_2O$, and $La(NO_3)_3{\cdot}6H_2O$ were dissolved in deionised water and added to a gel prepared by mixing equimolecular amounts of citric acid (99.5%) and ethylene glycol (99.5%) as a polydentate ligand. The excess water was slowly removed on a hot plate until a viscous liquid was obtained. Subsequently, the final slurry was slowly heated in air (1 °C min^{-1}) from room temperature up to 700 °C and kept at this temperature for 4 h. These conditions are essential to obtain a crystalline material.

b. Characterisation

XES/HERFD measurements were performed on the scanning branch of the I20 beamline at the Diamond Light Source, Didcot, UK. Measurements were taken using a Si(111) four-bounce monochromator using a high-resolution X-ray emission spectrometer.[10] For this experiment, the spectrometer was equipped with three Ge(440) analysers to allow the Kβ spectra to be measured.[10] Mn K-edge XES spectra were fitted using three Voigt functions which represent the $K\beta_{1,3}$, $K\beta_x$ and Kβ′ peaks.[11] Prior to the fitting, spectra were normalized, and linear background was subtracted. During the fitting, peak splittings were kept constant at theoretical values;[12] (i) splitting between $K\beta_{1,3}$ and Kβ′ peaks ≈ 14–16 eV and (ii) $K\beta_x$ was lower than main, $K\beta_{1,3}$, peak by ∼3 eV. The same fitting procedures were applied on spectra taken for Mn standard materials for comparison purposes. HERFD were measured by scanning the incident energy and detecting the fluorescence intensity at the maximum of the Mn $K\beta_{1,3}$ emission line with time resolution of ∼20 min per spectrum with 3 spectra collected. Data processing, background submission and normalisation was performed using Athena package. *In situ* XRD ball milling was performed at the ID15A beamline at the European Synchrotron Radiation Facility using a modified MM200 Retsch mill reported by Halasz *et al.*[13,14] The set-up comprised of a PMMA milling jar containing one 5 mm WC milling media with Mn_2O_3 and La_2O_3 precursor powders. The mill operated at 30 Hz for ∼19 h. The *in situ* XRD was collected at 69 keV, λ = 0.17971 Å with a beam size of 300 × 300 μm^2. A Dectris Pilatus X area detector was used with an exposure of 5s and a readout time of 120 s. The incident wavelength and detector distance (430 mm) were calibrated using a NIST CeO_2. The Raw data frames were integrated using the internal ESRF Matlab.Eva 5.0.0.22/PDF-4+ 2020 software package was used for phase identification and data plotting. *In situ* high pressure EDE-XAFS were performed at I20-EDE, the energy dispersive beamline at the Diamond Light Source, Didcot, UK. Energy-dispersive EXAFS was performed at the Mn K-edge (6539 eV) in transmission mode using a Si(111) polychromator. A diamond anvil cell (DAC) was fitted with 0.5 mm thick diamonds in order to reduce the diamonds absorption and enable XAS measurements at the Mn K-edge. The single-crystal diamond mini-anvils were mounted on fully perforated diamonds. Pressure was measured by the ruby fluorescence method.[15] The dispersive X-ray beam was focussed on the sample in the DAC with a spot size of 0.05 mm diameter. Diamond single crystal reflections were deglitched following a similar procedure to Hong *et al.*[16] Spectra were recorded every 2 GPa of pressure. XRD was collected on a Bruker AXS D8 diffractometer with Cu Kα radiation over a range of 2θ = 10–130° with 0.044° step size (Johnson Matthey, Sonning Common, UK). Phase identification was performed using Bruker-AXS Diffrac Eva V4.2 with Rietveld refinement performed using Bruker-AXS Topas 4.2. XAS measurements were performed at the B18 Beamline, Diamond Light Source. XAS measurements at the Mn K-edge (6539 eV) and La L_3-edge (5483 eV) were performed in transmission mode using QEXAFS setup with fast scanning Si(111) double crystal monochromator. An appropriate foil was placed between I_t and I_{ref} and measured concurrently with XAS spectra acquisition. At the Mn K-edge XAS spectra was acquired with a time resolution of 20 min per spectrum (k_{max} = 14) averaged over 3 scans. At the La L_3-edge XAS spectra were acquired with a time resolution of 5 min per spectrum (k_{max} = 10) averaged over 3 scans.

Open Access Article. Published on 30 Qasa Dirri 2020. Downloaded on 22/04/2026 6:39:19 AM.
This article is licensed under a Creative Commons Attribution 3.0 Unported Licence.

Data processing was background submission and normalisation was performed using Athena and Artemis software package.[17,18] XPS was carried out with a Thermo Escalab 250. The radiation used was monochromatised aluminium Kα radiation with a 650 μm spot size. Charge compensation was provided by the in-lens electron flood gun at a 2 eV setting and the "401" unit for "zero energy" argon ions. Sensitivity factors after Scofield used in quantification performed by Johnson Matthey, Sonning Common, UK.

c. Catalytic activity (deN_2O)

DeN_2O was carried out in a fixed-bed quartz reactor (Hiden CATLAB) with the temperature range of 100–800 °C, using a ramp rate of 10 °C min^{-1}. The reaction was performed at 30 mL min^{-1} flow of 0.5% N_2O in He over 400 mg of catalyst with sieve fraction 125–250 μm to result in a GHSV = 18 000 h^{-1}. The exhaust gases composition was measured using a Hiden QGA mass spectrometer for He (m/z = 4), N_2 (m/z = 28), O_2 (m/z = 32), N_2O(m/z = 46).

d. *In situ* NAP-XPS deN_2O

The catalytic reaction was performed on 3 samples; mechanochemically prepared $LaMnO_3$, milled under air and argon gas atmospheres for 4 h, and compared to sol–gel synthesised $LaMnO_3$.

NAP-XPS was performed at the beamline B07-C (VerSoX) at the Diamond Light Source. Spectra were recorded at the La 3d, Mn 2p, O 1s, C 1s and Mn 3s levels at 834.5–855 eV, 641–655 eV, 529–532 eV, 284–289 eV and 82–89 eV binding energies, respectively, during the deN_2O. Samples were pressed into 8 mm pellets containing 50 mg of $LaMnO_3$. The reaction was performed under 0.5% N_2O in He, with scans performed at room temperature in vacuum, room temperature with 10 mbar of N_2O and then subsequently at 400 °C and 600 °C (still under 10 mbar of N_2O). The measurements were performed at specific incident energies for each XPS region to ensure the same kinetic energy/depth of the emitted electron (~350 eV). To achieve a variable depth profile the Mn 3s region was recorded with an incident energy of 1200 eV. Each XPS region was aligned to a reference C 1s peak at 284.8 eV[19] to compensate for charging effects. Peak positions and FWHM determined after using Shirley background subtraction on CasaXPS, with all residual standard deviations of the curve fitting reported to be under 1.

3. Results and discussion

3.1 Understanding the mechanochemical synthesis of $LaMnO_3$

3.1.1 HERFD-XANES. XAS benefits from analysing both the amorphous and crystalline content, as it does not rely on periodic ordering, to give a combined bulk structure. Performing XAS at both the Mn K-edge and La L_3-edge on *ex situ* time-slices during the mechanochemical synthesis of $LaMnO_3$ allowed for further insights into the mechanochemical synthesis of $LaMnO_3$, which suggested that initially La dispersed over Mn_2O_3 as soon as 1 h of milling. However, traditional Mn K-edge XAS spectra often results in broad features in the XANES region (Fig. 1). The major cause of this is the lifetime of the core-hole that is created during the excitation of the 1s electron.[20] There is also the added

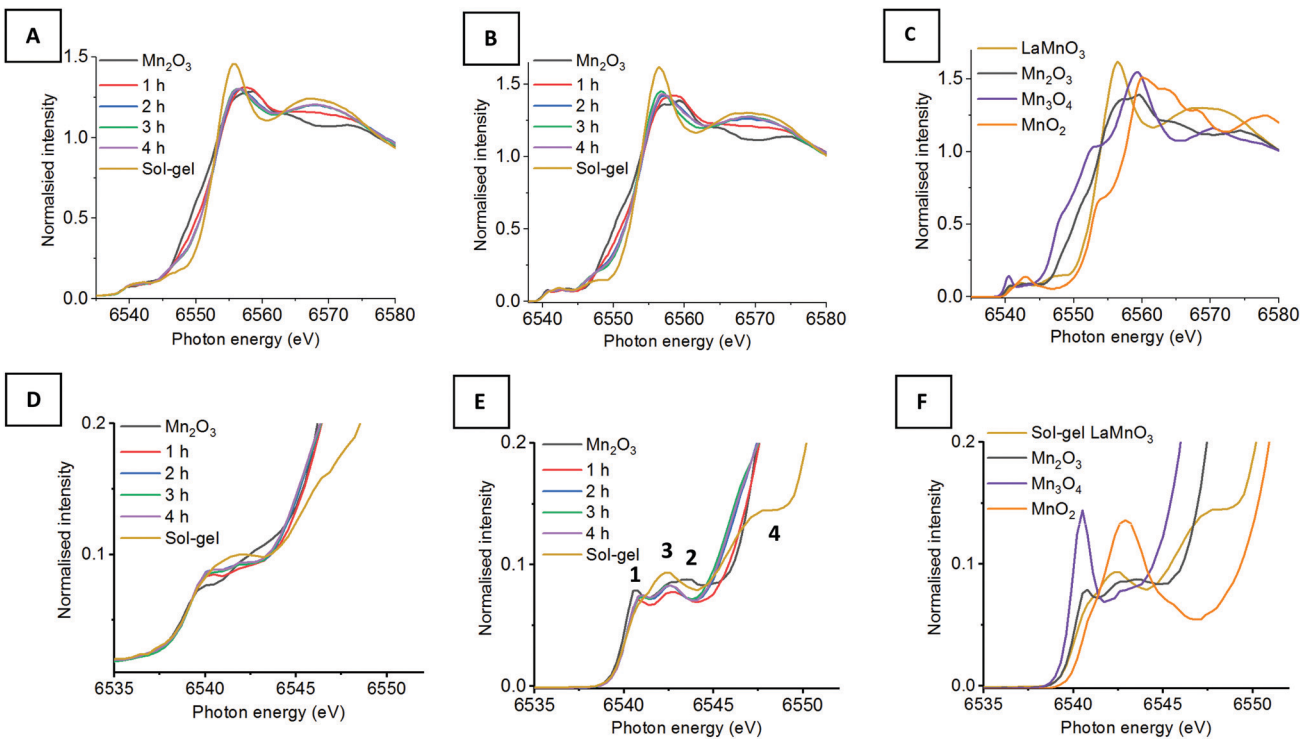

Fig. 1 (A) XAS Mn K-edge XANES compared to (B) HERFD-XANES of time-slices during the mechanochemial synthesis if $LaMnO_3$ compared to (C) reference Mn(II), (III), (IV) oxides and sol–gel synthesised $LaMnO_3$ with (D–F) their respective highlighted pre-edge region.

 This journal is © the Owner Societies 2020

Open Access Article. Published on 30 Qasa Dirri 2020. Downloaded on 22/04/2026 6:39:19 AM.
This article is licensed under a Creative Commons Attribution 3.0 Unported Licence.

complication of the overlap of multiple transitions. The different transitions arise as a consequence of both local and non-local excitations; *i.e.* there is promotion to the hybridised orbitals located on the absorber or there is charge transfer to a neighbouring site.[7] This study has collected HERFD-XANES using the $K\beta_{1,3}$ emission line, which probes the decay from 3p → 1s, to assess the changes to the electronic structure of the milled materials as a function of milling time.

Fig. 1 shows the XANES and HERFD-XANES data, with expanded pre-edge regions for the milled materials and the Mn oxide reference compounds. Assessing the Mn K-edge HERFD-XANES, the level of spectral resolution has vastly improved compared to the conventional XANES data. This increased resolution is more clearly pronounced in the pre-edge region, which shows more defined transitions that are well separated from the main edge. The HERFD-XANES spectra of the reference Mn oxides (Mn_2O_3, Mn_3O_4, MnO_2 and $LaMnO_3$) and their interpretation allow for an increased understanding of the ball milled intermediates and final material.

For the $K\beta_{1,3}$ HERFD-XANES data the main edge results from an allowed 1s → 4p transition. The position of this main edge transition is dependent on the oxidation state of the system; an increased formal charge on the Mn results in the transition shifting to higher energy. In the pre-edge region, there are multiple transitions that give rise to the complex structure observed. The 1s → 3d transitions, that are normally forbidden by dipole selection rules, in this region can be quadrupolar or dipolar in nature, dependent on the local mixing of 3d/4p wavefunctions and the presence of non-local excitations; these occur with 3d states of neighbouring metal sites, through an oxygen-mediated intersite hybridisation, *e.g.* Mn(4p)–O(2p)–Mn′(3d).[21] The size and shape of the pre-edge peaks is therefore highly dependent on the geometry of central absorbing atom.[7]

Assessing the pre-edge region for Mn_2O_3 two clear peaks can be observed at 6540.8 eV and 6543.0 eV. These different features arise as a consequence of the structure of Mn_2O_3 that contains two different Mn(III) coordination sites. Both sites are 6 coordinate, with respect to oxygen, however, one site adopts a more regular centrosymmetric O_h geometry, whereas the other displays a large degree of Jahn–Teller distortion. The work by Farges showed that the lower energy peak can be assigned to the centrosymmetric Mn site and the higher energy peak to the Jahn–Teller distorted Mn site.[22] This can further be applied to the pre-edge features for the mixed valent Mn_3O_4, which contains both Mn(II) and Mn(III). The intense peak at 6540.5 eV results from the tetrahedrally coordinated Mn(II), allowing for 3d–4p local hybridisation, resulting in an intense dipole transition. A low intensity peak is also observed at 6542.6 eV, originating from Mn(III). It should be noted that the intensity of these two peaks, at 6540.5 eV and 6542.6 eV, do not relate to the proportion of Mn(II) and Mn(III). Work by Radu *et al.* shows the Mn(II) peak as a single feature, with the Mn(III) feature extending below the Mn(II) peak due to the multiplet effect of the final state ($1s^13d^5$).[23] For MnO_2, the Mn(IV) cation is positioned in an octahedral site, however, the pre-edge for Mn(IV) is extremely complex and even HERFD-XANES struggles to resolve the features.[22] Previous work shows that the broad feature observed at 6542.9 eV is a combination of 1s → 3d quadrupole transitions and non-local excitations.[22]

$LaMnO_3$, synthesised here by the Pechini method,[24] has two peaks in the pre-edge region observed at 6542.3 eV and (a shoulder at) 6547.7 eV. The peak at 6542.3 eV has been demonstrated to be two overlapping peaks from both a 1s→ 3d quadrupole transition and a 1s → 3d4p non-local transition. This non-local transition occurs from the 3d states of neighbouring metal sites, Mn(4p)–O(2p)–Mn′(3d), through the vertex linked octahedral units.[25] The shoulder observed at 6547.8 eV is often overlooked within the Mn K-edge XANES of $LaMnO_3$. However, work by Ignatov *et al.* showed they could not effectively model this shoulder within $LaMnO_3$ XANES without considering the contribution of d and f orbitals, suggesting this shoulder arises due to Mn 4p and La 5d hybridisation.[26]

Using this analysis of reference Mn oxides we can now effectively assess the changes within the pre-edge region of Mn during the evolution of $LaMnO_3$ by mechanochemical synthesis. After 1 h of milling there are already clear differences in the HERFD-XANES spectrum compared to Mn_2O_3. The key differences are a decrease in intensity of the transitions at (1) 6540.8 and (2) 6543.0 eV. These changes provide important information about the chemical steps occurring during the milling process. The decrease in intensity of the transition at (2) indicates that the extended crystallites of Mn_2O_3 have been significantly disrupted; the transition is a non-local excitation to a neighbouring site and its reduced intensity is clear evidence for less extensive Mn–O–Mn interactions. The decrease in the transition at (1) indicates that there has been alterations to the local geometry of Mn sites. On increasing milling time to 2 h, there is then an increase in intensity of the transitions associated with $LaMnO_3$ at (3) 6542.3 eV, indicating that there are changes to the local structure indicative of the formation of a perovskite unit. There are no further discernible changes in the spectra for milling times of 2–4 h. Comparing the final ball milled, $LaMnO_3$, to the sol–gel reference, clear differences are observed, most noticeably lower intensity transitions at (3) and (4) at 6547.7 eV.

The peak at (3) is assigned to a 1s → 3d4p non-local hybridised transition to neighbouring Mn sites, the strength of this transition is dictated by the metal–oxygen bond length and the metal–oxygen–metal bond angle.[27] The strongest transition, and ideal hybridisation, is achieved by a short bond length and a linear bond angle.[25] In our previous study, the Mn–O bond lengths calculated by EXAFS for both the sol–gel and mechanochemically prepared $LaMnO_3$ have comparable distances within the error range of the technique. Moreover, the final ball-milled $LaMnO_3$ is a complex mixture of both amorphous and crystalline content, consistent with multiple metal–oxygen–metal bond angles. The crystalline $LaMnO_3$ has a more linear metal–oxygen–metal bond angle and it has a higher intensity peak for this transition at (3). Furthermore, the absence of the shoulder at (4) for the ball milled materials suggests the lack of Mn4p La5d hybridisation.[26] In our previous work, we reported that the EXAFS fitting model for the ball milled material required two Mn–La scattering paths at 3.24(1) Å and 3.37(1) Å, which is significantly different to that observed for the crystalline sol–gel sample. These changes in

Open Access Article. Published on 30 Qasa Dirri 2020. Downloaded on 22/04/2026 6:39:19 AM.
This article is licensed under a Creative Commons Attribution 3.0 Unported Licence.

Mn–La coordination have disrupted the Mn 4p La 5d hybridisation and affect the transition at (4).

3.1.2 XES. The assessment of the HERFD-XANES pre-edge region has provided a greater detailed understanding of changes to the local geometry during the mechanochemical synthesis of $LaMnO_3$ and the differences compared to the sol–gel synthesised perovskite. The pre-edge features suggest a purely Mn(III) state within the ball milled materials, with no Mn(II) or Mn(IV) features observed. However, as we have seen, the XANES is strongly influenced by the local geometry around the absorbing atom and this needs to be accounted for when assessing oxidation state. We now detail Mn $K\beta_{1,3}$ emission spectroscopy in order to obtain more reliable information on the Mn charge during the mechanochemical synthesis.

Fig. 2 shows the Mn Kβ mainlines, consisting of a strong Mn $K\beta_{1,3}$ peak and with a Mn Kβ′ satellite at a lower energy, for the 3p → 1s transition of reference Mn oxides and a sol–gel synthesised $LaMnO_3$. The splitting of these peaks originate from the strong coupling interaction between the 3p hole and the total spin of the 3d electrons.[28,29] Any energy shifts of the Mn $K\beta_{1,3}$ peak is expected to result from a combination of effective nuclear charge (Z_{eff}) and spin state. Work by Beckwith *et al.* showed that for Mn complexes the Z_{eff} and 3d spin effects oppose one another.[30] Therefore, an increase in oxidation state corresponds to an decrease in total spin, which tends to shift the Mn $K\beta_{1,3}$ to a lower energy.[21]

This is strongly reflected in the Mn reference materials reported here, which have fitted Mn $K\beta_{1,3}$ peaks for MnO_2, Mn_2O_3 and M_3O_4 species at 6490.26, 6490.66 and 6490.73 eV, respectively (Table 1) (Fig. S1, ESI†). When considering the reference sol–gel synthesised $LaMnO_3$, the fitted Mn $K\beta_{1,3}$ peak position is reported at 6490.55 eV. This indicates that the Mn(III) oxidation state shows a small variation in the Mn $K\beta_{1,3}$ peak position.

Assessing the position of the fitted Mn $K\beta_{1,3}$ peak for reference Mn oxide materials as a function of oxidation state allows us to extract oxidation state information (Fig. 2C). The positions of the Mn $K\beta_{1,3}$ emission lines suggests that the milled materials have an average oxidation state higher than the Mn(III) oxidation state expected. This is consistent with our previous XPS analysis which identified Mn(IV) at the surface of the mechanically prepared $LaMnO_3$. However, there is an associated error in determining the positions of deconvoluted peaks. When this is taking into consideration, alongside the variance Mn(III) reference materials (Mn_2O_3 and sol–gel $LaMnO_3$), all that can be reliably confirmed is that the net oxidation state for all milled samples is very similar to that of the sol–gel prepared $LaMnO_3$.

Table 1 Mn $K\beta_{1,3}$ peak positions for reference Mn oxides and sol–gel synthesised $LaMnO_3$ compared to 'time-slices' throughout the mechanochemical synthesis of $LaMnO_3$

Compound	$K\beta_{1,3}$ max (eV)	Oxidation state
MnO_2	6490.26	IV
Mn_2O_3	6490.66	III
Mn_3O_4	6490.73	II/III
Sol–gel $LaMnO_3$	6490.55	III
1 h of milling	6490.57	3.0–3.3
2 h of milling	6490.53	3.0–3.3
3 h of milling	6490.54	3.0–3.3
4 h of milling	6490.56	3.0–3.3

3.1.3 Investigating the formation of $LaMnO_3$ by *in situ* milling and high pressure studies on La_2O_3 and Mn_2O_3. We have used *ex situ* analysis to provide further insights into the mechanochemical synthesis of $LaMnO_3$. Though *in situ* milling has been successfully monitored in real-time using XRD on materials such as MOFs with a vibrational mill and a PMMA jar, it was not possible to observe the evolution of the perovskite phase $LaMnO_3$ using this set-up (Fig. 3) with phase ID reporting only La_2O_3, $La(OH)_3$ and Mn_2O_3 diffraction peaks after ~19 h of milling.[14]

Mechanochemistry results in extremely localised high temperature and pressure spots on the powdered materials due to collisions between milling media and the milling jar.[31,32] High thermal synthesise (1300–1500 K), known as the ceramic method, is commonly known as a traditional preparation method for perovskites and are already well documented in literature.[33,34] Though high pressures have been applied to already synthesised mixed metal oxides, there is limited information on using pressure alone to synthesise the $LaMnO_3$ phase.[35,36] In order to mimic the forces transferred to the powdered materials through

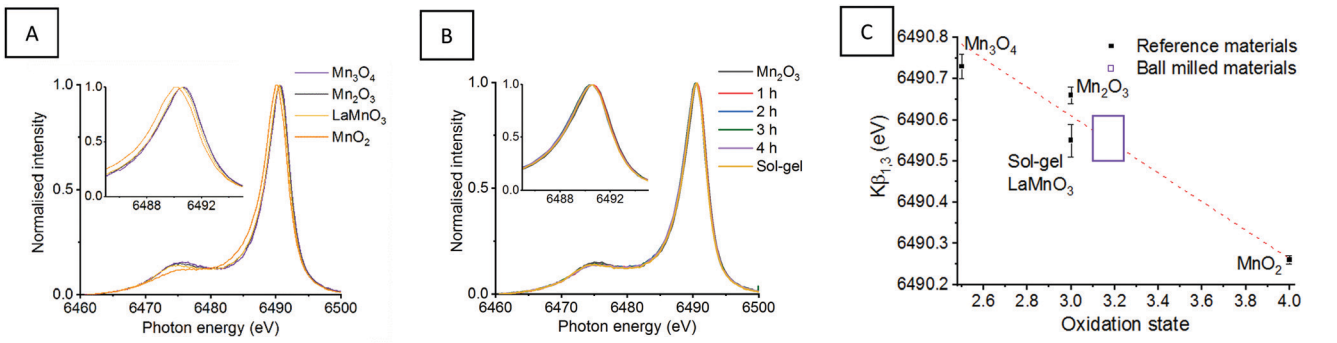

Fig. 2 Mn Kβ XES mainlines for (A) Mn reference oxides and sol–gel synthesised $LaMnO_3$ with (B) 'time-slices' during the mechanochemical synthesis of $LaMnO_3$ (C) presents the $K\beta_{1,3}$ max as a function of oxidation state, with a line of best fit calculated from the reference materials and used to calculate the oxidation state of the ball milled materials.[11]

 This journal is © the Owner Societies 2020

Open Access Article. Published on 30 Qasa Dirri 2020. Downloaded on 22/04/2026 6:39:19 AM.
This article is licensed under a Creative Commons Attribution 3.0 Unported Licence.

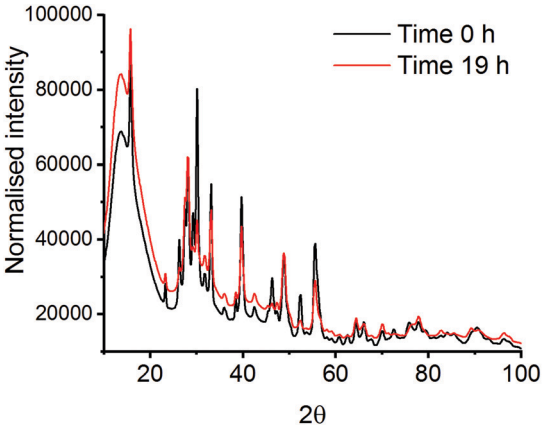

Fig. 3 XRD patterns at time 0 h and time 19 h after milling La_2O_3 and Mn_2O_3 with a PMMA vibrational mill.

the mechanochemical action of the mill, *in situ* high pressure studies using a diamond anvil cell (DAC) have been monitored by energy-dispersive-EXAFS (EDE) at the Mn K-edge. Systematic studies were performed on homogeneous mixtures of La_2O_3 and Mn_2O_3 up to pressures of 30 GPa at room temperature. Even at the highest pressure achieved with the perforated DAC, on mixtures that had been ball milled for 30 min, no significant changes in the EDE spectra were observed (Fig. 4). This indicates that either higher pressures or a combination of increased pressure and temperature are needed to mimic the conditions that drive mechanochemical transformations. Ultimately, this information combined with the results from the *in situ* vibrational mill, confirms that the mechanochemical synthesis of these metal oxide systems are extremely complicated to monitor *in situ*.

3.2 Comparison of milling environment

The La oxide precursor is significantly hydroscopic and readily forms a hydroxide on exposure to air. To understand the effect this change of precursor has on the final milled material, we have conducted the milling procedure in an inert atmosphere of argon.[37] The mechanochemical production of $LaMnO_3$ under argon was performed for 4 h, with the final material then subsequently exposed to air.

The XRD data was analysed using Rietveld refinement[38] to confirm the fraction of crystalline phases in the final milled material (Fig. 5). The data confirmed that for the mechanochemically prepared $LaMnO_3$ under inert conditions a milling time of 4 h was not sufficient to achieve complete conversion to perovskite $LaMnO_3$, with 77% crystalline perovskite calculated (100% was achieved when milling in air). The residual 23% comprises unreacted crystalline precursor phases. Here, the excess moisture/oxygen present in the milled material prepared in air is clearly beneficial in forming a crystalline final product.

To assess the crystalline and amorphous content of the argon milled $LaMnO_3$ EXAFS analysis was also performed (Fig. 6) (Table S1, ESI†). The argon milled $LaMnO_3$ EXAFS data is well modelled, using a single Mn–O and two Mn–La scattering paths. The two Mn–La scattering paths were calculated to be 3.13 Å and 3.30 Å, similar to that found for the air milled $LaMnO_3$; the shorter and longer distance La–Mn scattering paths arise due to amorphous and crystalline content, respectively. In general the EXAFS data of the air and argon milled samples are similar, however, there are differences in the Fourier transform resulting from changes in the amorphous/crystalline LaMn phases present. This model also exhibits a degree of oxygen deficiency, as with the air milled sample. To further investigate this, HERFD-XANES and Mn Kβ XES studies have been performed.

As seen in Section 1.1, broad unresolved features are observed within the traditional XANES, with HERFD-XANES showing a much greater resolution (Fig. 1). Fig. 7 shows the XANES and HERFD-XANES data, with expanded pre-edge regions for $LaMnO_3$ catalysts synthesised by mechanochemistry (in air and argon) and sol–gel, compared to the Mn_2O_3 precursor. The argon milled sample clearly shows an unshifted peak (1) at 6540.8 eV, which arises as a consequence of unreacted Mn_2O_3. The absence of peak (2) and the presence of peak (3) at 6542.6 eV suggest the formation

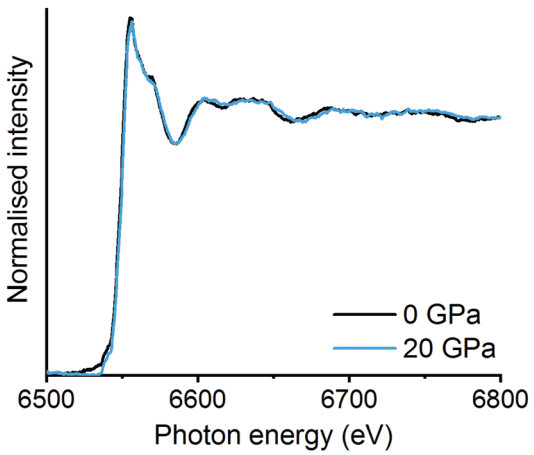

Fig. 4 *In situ* high pressure EDE spectra at 0 GPa and 20 GPa on La_2O_3 and Mn_2O_3 mixture after high energy ball milling for 30 min.

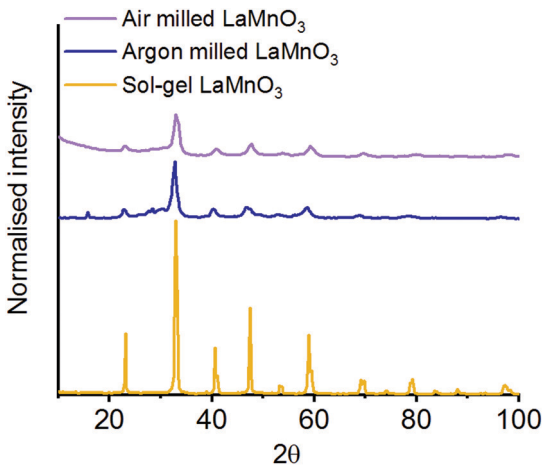

Fig. 5 XRD patterns $LaMnO_3$ mechanochemically synthesised 4 h under atmospheric and inert (argon) conditions compared to the sol–gel synthesised perovskite.

Open Access Article. Published on 30 Qasa Dirri 2020. Downloaded on 22/04/2026 6:39:19 AM.
This article is licensed under a Creative Commons Attribution 3.0 Unported Licence.

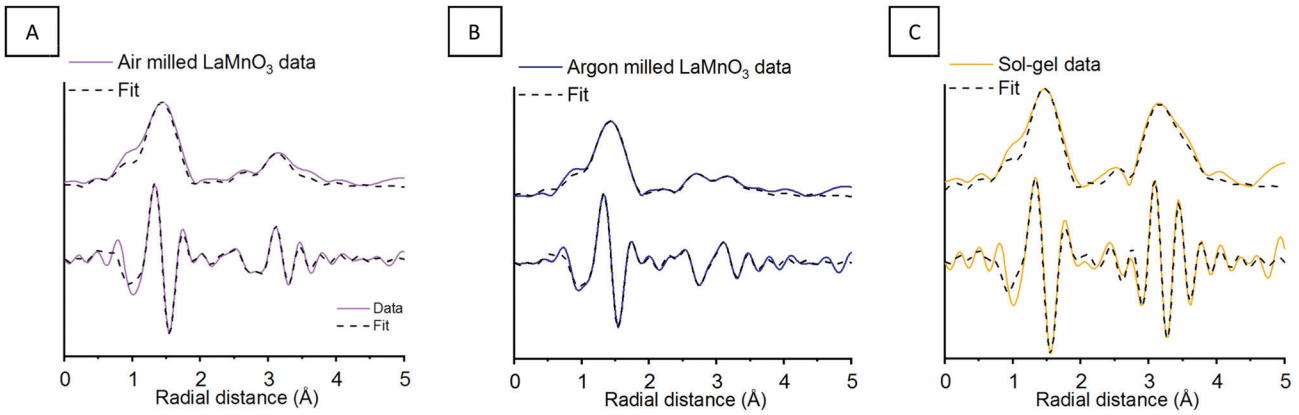

Fig. 6 Mn K-edge EXAFS data after 4 h of milling in (A) atmospheric and inert (B) milling conditions showing the magnitude and imaginary components of the k^2-weighted FT data and fits compared to (C) sol–gel synthesised $LaMnO_3$.

of perovskite-like structures; peak (3) resulting from a transition to the non-local neighbouring Mn sites within perovskites. The decrease in intensity of peak (3) is indicative of a greater proportion of structural disorder. Furthermore, the argon milled material lacks the shoulder (4) at 6547.8 eV, suggesting an absence of Mn 4p La 5d hybridisation.[26] In the EXAFS model the argon milled $LaMnO_3$ lacks the longer scattering path of 3.70 Å present in the sol–gel prepared material (Table S1, ESI†). This further suggests that the changes in the Mn–La coordination have disrupted the Mn 4p La 5d hybridisation and have affected the transition at 6547.8 eV.

The observed shift in the main edge for the argon catalyst could suggest a reduction in Mn charge. However, the edge position at the Mn K-edge is not a suitable measure for oxidation state as geometry and symmetry effects also dominate the XANES and therefore $K\beta_{1,3}$ emission spectroscopy has been performed in order to achieve more reliable information.

Using the fitting analysis stated in Section 3.1.2, the Mn Kβ mainlines have now been assessed for the argon milled $LaMnO_3$, compared to the air milled and sol–gel prepared perovskite (Fig. 8) (Fig. S3, ESI†). Both air and argon milled $LaMnO_3$ have fitted Mn $K\beta_{1,3}$ peak positions within error of one

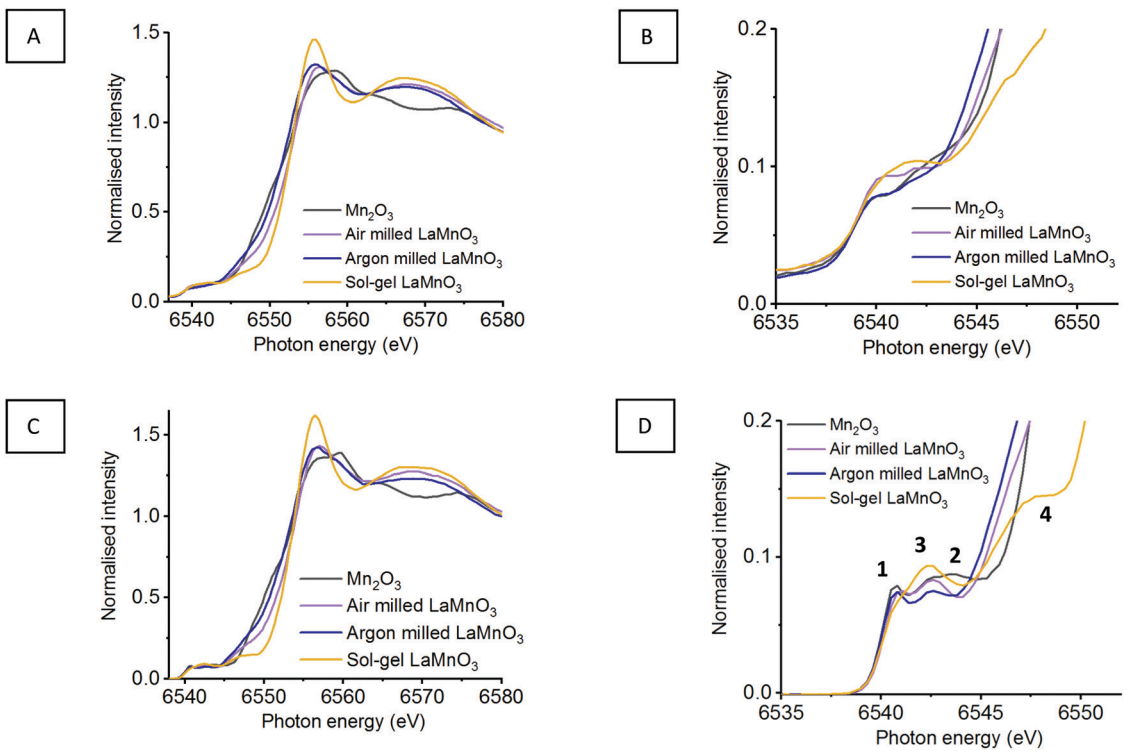

Fig. 7 (A) Mn K-edge XANES with (B) highlighted pre-edge region compared to (C) HERFD-XANES with (D) highlighted pre-edge region of mechanochemial synthesis if $LaMnO_3$ within air and argon environments compared to sol–gel $LaMnO_3$ and precursor Mn_2O_3.

Open Access Article. Published on 30 Qasa Dirri 2020. Downloaded on 22/04/2026 6:39:19 AM.
This article is licensed under a Creative Commons Attribution 3.0 Unported Licence.

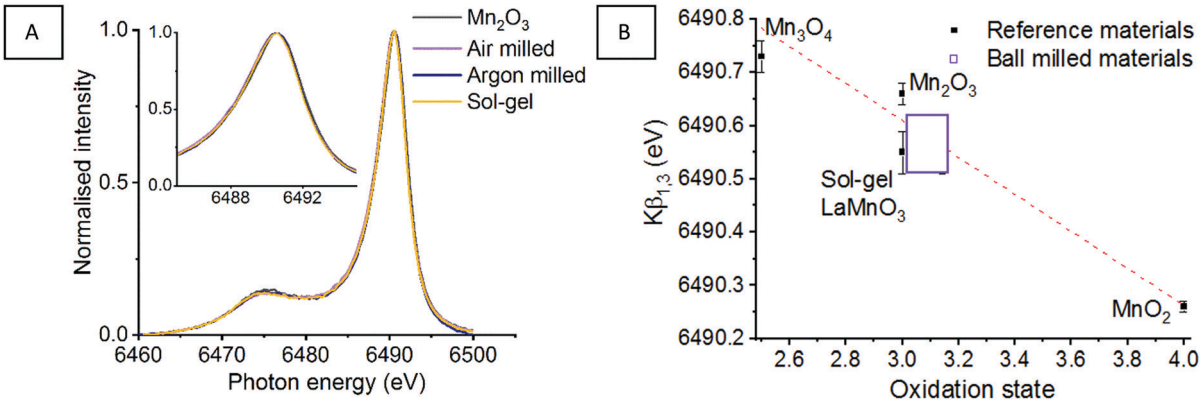

Fig. 8 (A) Mn Kβ XES mainlines of time-slices through the mechanochemical synthesis of $LaMnO_3$ from precursors La_2O_3 and Mn_2O_3 along with (B) which presents the $K\beta_{1,3}$ max as a function of oxidation state, with a line of best fit calculated from the reference materials and used to calculate the oxidation state of the ball milled materials.[11]

another, which is consistent with the sol–gel $LaMnO_3$, as stated earlier.

Previously, we reported the importance of assessing the surface of the $LaMnO_3$ catalysts to identify possible active sites for catalysis by X-ray photoelectron spectroscopy (XPS).[5] The atomic percent ratios of La, Mn and O species at the surface of $LaMnO_3$ show the argon milled to have higher ratio of La to Mn on the surface compared to the air milled and sol–gel synthesised samples (Table S2, ESI†). Fig. 9A shows the O 1s XPS signals of mechanochemically and sol–gel synthesised $LaMnO_3$. The argon milled sample follows a vastly different spectral profile compared to that of both the air milled and sol–gel synthesised $LaMnO_3$. Previously, we reported using curve fitting to assess the change in adsorbed species on the catalyst surface.[5]

Using curve fitting here, three features were deconvoluted within the O 1s XPS region at 529.3–529.6 eV, 531.1–531.7 eV and 533.4–535.0 eV. The lowest energy binding peak at 529.3–529.6 eV is assigned to lattice-type oxygens in the perovskite (O_2^{2-}), with the peak at 531.1–531.7 eV assigned to adsorbed species, such as O^{2-}, O^- or OH^-.[39–41] The peak at ~533.5 eV corresponds to adventitious carbon, with analogous C–O peaks confirmed within the C 1s XPS region at 286.2 eV and 288.6 eV.[39–41]

Commonly it is assumed that active oxygen species adsorb on the surface to compensate for lattice oxygen vacancies.[41] Firstly, the Brunauer–Emmett–Teller (BET) surface areas were calculated to be within range of one another; ~5 $m^2\ g^{-1}$ for the ball milled samples and ~8 $m^2\ g^{-1}$ for the sol–gel $LaMnO_3$. Therefore, comparing the adsorbed oxygen to lattice oxygen can give an indication of the changes to adsorption centres, independent of surface area.[42–44] The argon milled sample shows a greater intensity for the higher energy binding peak, indicating more adsorbed species on the surface compared to the other $LaMnO_3$ samples. The relative intensity of the adsorbed oxygen feature decreases in the order; argon milled >4 h milled ≈ sol–gel preparation.

The XPS Mn 3s region spectra (Fig. 9B) indicate a mixed Mn oxidation state with peak splitting at 4.8–5.0 eV suggesting the presence of Mn(IV) and Mn(III) species (Table S3, ESI†). Analysis in the La 3d region (Fig. 9C) indicate a 3+ oxidation state for all samples, however, the argon milled $LaMnO_3$ presents a different multiplet splitting (Table S3, ESI†). A reduced multiplet splitting of 3.7 eV is indicative of $La(OH)_3$ species, consistent with the higher surface ratio of La (Table S2, ESI†), and the higher percentage of adsorbed species, –OH, within the O 1s region. This XPS analysis signifies the importance of surface sensitive techniques, as well as bulk structure analysis, XAS and XES, in order to understand how different synthetic routes effect the structural and catalytic properties of these $LaMnO_3$ catalysts.

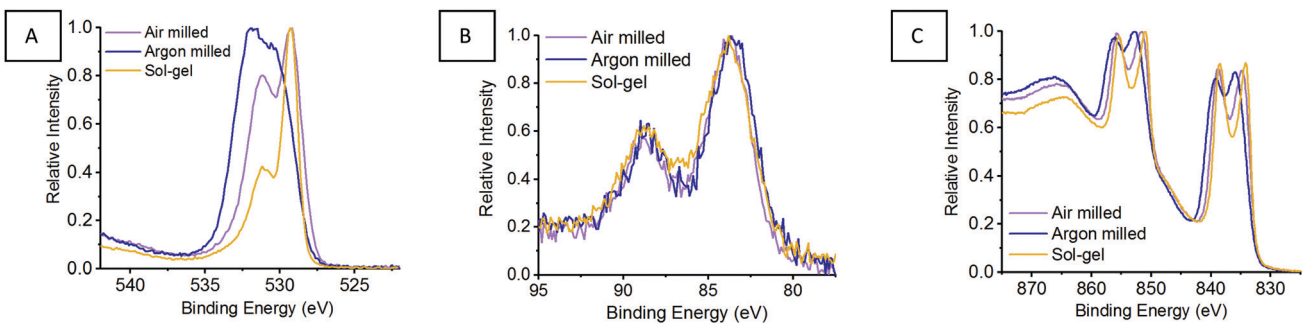

Fig. 9 XPS in the (A) O 1s, (B) Mn 3s and (C) La 3d region for $LaMnO_3$ synthesised by sol–gel and mechanochemistry with air and argon environments.

Open Access Article. Published on 30 Qasa Dirri 2020. Downloaded on 22/04/2026 6:39:19 AM.
This article is licensed under a Creative Commons Attribution 3.0 Unported Licence.

3.3 Catalytic testing

N_2O decomposition (deN_2O) has been performed on the differently synthesised $LaMnO_3$ catalysts, with the light-off temperature curves detailing the percentage conversion of N_2O to N_2 (Fig. 10). Good reproducibility of this performance is shown in Fig. S4 (ESI†). Air milled and the sol–gel synthesised $LaMnO_3$ show similar activity, which begins ~350 °C with 100% conversion achieved by 550 °C. The argon milled $LaMnO_3$, however, shows activity starting below 300 °C. This indicates that the catalytic activity cannot be explained by analysis of the bulk structures alone, as both ball milled catalysts show similarities in structure by HERFD-XANES and XES. The surface analysis of the O 1s region by XPS, however, indicates changes at the surface for the argon milled $LaMnO_3$. With the desorption of oxygen well understood to be the rate controlling step within the mechanism of deN_2O this supports our previous work, that proposes the higher amount of surface adsorption centres is linked to a higher conversion of N_2O to N_2 at lower temperatures.[5,45,46] Furthermore, this argon milled catalyst shows a change in the light-off curve at 550 °C, which has previously been correlated to an increase in crystalline perovskite phase for other ball milled species during deN_2O. Here, the high reaction temperatures have resulted in annealing of the ball milled perovskite, changing the catalyst structure and thus the catalytic activity (Fig. S5, ESI†). However, the argon milled catalyst still shows to be largely effective at lower temperatures, before the phase transformation takes place.

Furthermore, with XPS analysis showing the argon milled catalyst to have a higher proportion of La at the surface, it raises a very interesting feature as traditionally it is thought that the Mn is the active species for catalysis in this system.[47] Due to La electronic configuration it does not possess redox capabilities and is most stable in a 3+ oxidation state. However, differences do occur in the multiplet splitting within the XPS La 3d region, with the argon milled catalyst having a higher percentage of adsorbed oxygen species. In order to understand the role of La during deN_2O and how the other XPS regions are affected during the reaction *in situ* near ambient pressure (NAP)-XPS will now be discussed.

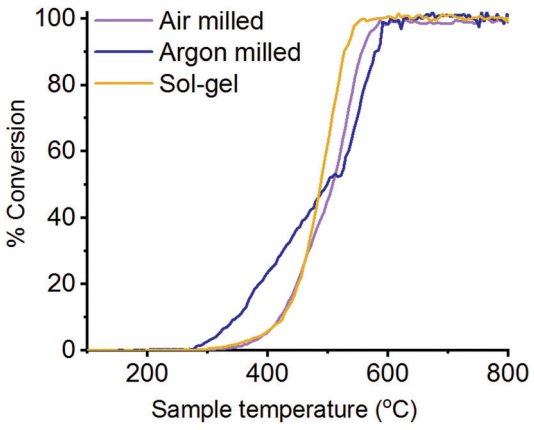

Fig. 10 Light-off curve of the percentage of deN_2O to N_2 over $LaMnO_3$ catalysts synthesised by mechanochemistry and sol–gel synthesised with 0.5% N_2O/He at 30 mL min^{-1} with a pre-treatment of He at 30 mL min^{-1}.

3.4 *In situ* NAP-XPS deN_2O

In the previous sections, we were able to link the catalytic activity towards deN_2O to the surface properties of the $LaMnO_3$ catalysts. It is critical to understand how the deN_2O process effects the surface properties and stability of our $LaMnO_3$ catalysts during N_2O adsorption, dissociation and desorption of N_2. Our previous lab-based XPS was performed under vacuum with a fixed incident beam. This *ex situ* analysis of the surface of the catalysts often presents vastly different properties compared to that under reaction conditions.[48] Furthermore, controlling the incident energy allows for the same specific penetration depth of the surface for each XPS region.[49] In this section, NAP-XPS has been performed under working conditions during deN_2O with spectra recorded at the La 3d, Mn 2p, and O 1s regions at 834.5–855 eV, 641–655 eV and 529–532 eV binding energies, respectively, for the differently synthesised perovskite catalysts (Fig. S6–S8, ESI†). To achieve a comparison depth profile the Mn 3s region was performed with a greater incident energy. With the argon milled $LaMnO_3$ catalyst showing promising activity at lower temperatures (Fig. 10) we now the detail the surface properties during *in situ* deN_2O compared to the other $LaMnO_3$ catalysts.

Initially, the Mn XPS regions (Mn 2p and Mn 3s) have been assessed for the argon milled $LaMnO_3$ with scans performed at RT under a N_2O atmosphere (Fig. 11A) and then after heating at 400 °C and 600 °C (Fig. S9, ESI†). Within the Mn 2p region two main peaks are observed at ~641.5 eV and ~653 eV, originating from spin–orbit coupling, assigned as Mn $2p_{3/2}$ and Mn $2p_{1/2}$ respectively.[50] These peak positions give an indication of the Mn oxidation state at the surface. Due to the broad and asymmetric nature of the peaks, deconvolution of both Mn $2p_{3/2}$ and Mn $2p_{1/2}$ peaks by curve fitting resulted in a total of four peaks for the region, suggesting mixed valency. The deconvoluted peak positions at RT in N_2O for Mn $2p_{3/2}$ were recorded at 641.5 and 643.2 eV and for Mn $2p_{1/2}$ at 653.3 and 655.6 eV representing Mn(III) and Mn(IV), respectively (Table 2).[51–53] On subsequent heating to 400 °C and 600 °C the peak positions are observed to remain ±0.2 eV within each other. Assessing the area of the deconvoluted peaks within Mn $2p_{3/2}$ region can give an indication of the relative abundance of Mn(III) and Mn(IV) contributions (Table 2).[40] Calculating a ratio of the areas for each measurement results in consistent 1 : 1.3 ± 0.1 ratio of Mn(IV) : Mn(III) during *in situ* deN_2O for the argon milled catalyst.

Comparison of the argon milled catalyst to the air milled and sol–gel prepared $LaMnO_3$ shows that there are distinct variations of the initial Mn(IV)/Mn(III) peak positions and area contributions (Tables S4 and S5) (Fig. S10 and S11) (ESI†). However, on heating to 400 °C and 600 °C during deN_2O the Mn(IV)/Mn(III) ratios for all catalysts remain within ±0.2 of one another, with similar deconvoluted peak positions recorded.

 This journal is © the Owner Societies 2020

Open Access Article. Published on 30 Qasa Dirri 2020. Downloaded on 22/04/2026 6:39:19 AM.
This article is licensed under a Creative Commons Attribution 3.0 Unported Licence.

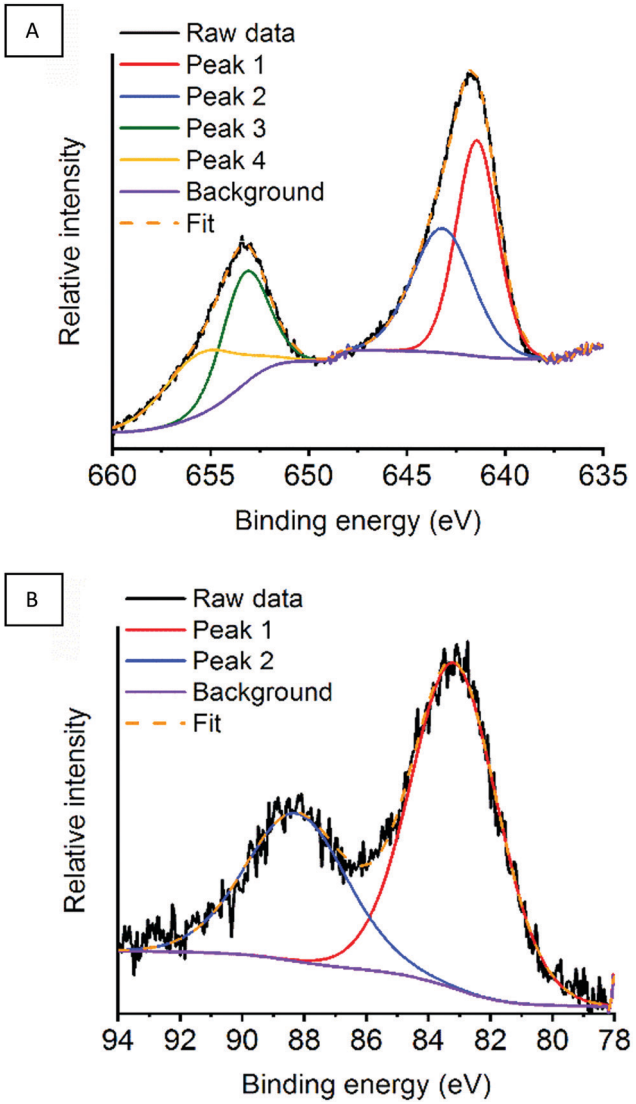

Fig. 11 (A) Mn 2p region and (B) Mn 3s region for the argon milled catalyst at RT under a N_2O atmosphere.

This is indicative of surface reactions occurring during catalysis that change the net oxidation state.

The Mn 3s region provides complimentary information and was recorded at an increased kinetic energy of ~770 eV, for enhanced depth profiling. The splitting of the Mn 3s peak (Fig. 11B) at ~83.5 and ~88.5 eV (Table 2) is a final state effect due to the parallel and anti-parallel coupling between the spins of the remaining 3s electron and the 3d electrons.[54] On increasing oxidation state, *i.e.* a decrease of d electrons, the separation between these two peaks is known to decrease.[55] For the argon milled catalyst a Mn 3s peak splitting value of 5.1 eV is observed at room temperature in vacuum. This suggests, a mixed Mn(IV)/Mn(III) valency, with literature reporting a peak splitting of 5.4 eV for Mn_2O_3 and 4.4 eV for MnO_2.[52,53] No change is observed for the Mn 3s peak splitting on the exposure to N_2O gas. However, on increasing temperature, this splitting increases to 5.4 eV, which is indicative of the Mn(III) oxidation state.[53] This increased depth-profiling observes the diffusion of sub-surface oxygen towards the exterior of the particle, which is responsible for the observed change in oxidation state.[56,57] The lattice oxygen that has migrated towards the surface is then available to participate in the deN_2O process.[58,59] With the mixed Mn(III) and Mn(IV) valences still observed at 600 °C at a lower depth penetration (Mn 2p region) it suggests this is a highly surface sensitive reaction.

This behaviour, of the splitting energy increase due to elevated temperatures, within the Mn 3s region was also found for the other $LaMnO_3$ catalysts (Tables S4 and S5) (Fig. S10 and S11) (ESI†). Understanding the Mn 2p and Mn 3s XPS regions highlights that, though the differently synthesised $LaMnO_3$ catalysts have varying bulk properties, at the surface there are similarities in how the Mn environment acts under working conditions.

The La 3d XPS region (Fig. 12 and Fig. S12, ESI†) shows the typical doublet splitting, with the lower energy doublet assigned to La $3d_{5/2}$ and the higher, La $3d_{3/2}$.[60] The peak splitting of the La $3d_{5/2}$ doublet has been used to understand the nature of the La species.[61] The asymmetric nature of the peaks within the La 3d region required three peaks to deconvolute each doublet (Fig. 12 and Fig. S12, ESI†).[62,63] For the argon milled catalyst, all the values of La $3d_{5/2}$ peak splitting during deN_2O are typical of La(III) compounds, which is further confirmed by the spin–orbit coupling values of 16.8–16.9 eV for all species (Table 2).[41] Initially, at RT under vacuum, the La $3d_{5/2}$ peak splitting of 3.9 eV is indicative of $La(OH)_3$ (Table 2). This is further confirmed by the presence of $La(OH)_3$ diffraction peaks in Fig. 5. Increasing the temperature during deN_2O results in an increase in the peak splitting value, suggesting the formation of an oxide species at the surface.[64]

Both the air milled and sol–gel $LaMnO_3$ start with a higher La $3d_{5/2}$ splitting value, of 4.1 eV and 4.2 eV respectively, compared to that of the argon milled catalyst, indicating a more oxide surface initially (Tables S4 and S5) (Fig. S13 and S14) (ESI†).[65] The ball milled samples record a decrease in the La 3d splitting on exposure to N_2O (~0.1 eV). This could be indicative that the adsorbed N_2O is interacting with surface La species.

Fig. 13 shows the deconvoluted fitted peaks for the O 1s region in argon milled $LaMnO_3$ at RT under a N_2O atmosphere and then at 600 °C (full data set Fig. S15, ESI†). On deconvolution of the O 1s region three oxygen species can be identified (Table 2). In Table 2, peak 1 is assigned to lattice-type oxygens (O_2^{2-}), peak 2 to adsorbed species such as O_2^-, O^- or OH^- and peak 3 and 4 is associated with adsorbed adventitious carbon or molecular water.[39–41]

By monitoring *in situ* deN_2O by NAP-XPS clear changes can be observed within the O 1s region for the argon milled catalyst, which have not been previously reported. Whilst remaining at RT, on the introduction of N_2O an increase in the proportion of adsorbed species can be observed, along with the presence of a higher binding energy peak 4 at 534.6 eV (Fig. S15A, ESI†). This is indicative that N_2O is adsorbed on the surface at room temperature, in agreement with La 3d XPS data. A change in

Open Access Article. Published on 30 Qasa Dirri 2020. Downloaded on 22/04/2026 6:39:19 AM.
This article is licensed under a Creative Commons Attribution 3.0 Unported Licence.

Table 2 NAP-XPS deconvoluted peak positions and areas during *in situ* deN_2O of the argon milled catalyst at Mn 2p, Mn 3s, La 3d and O 1s regions

		RT vacuum	RT in N_2O	400 °C in N_2O	600 °C in N_2O
Mn 2p	Peak 1	—	641.5, 46 205	641.3, 52 777	641.1, 63 001
	Peak 2	—	643.2, 39 338	643.3, 40 166	643.3, 44 761
	Peak 3	—	653.3, 26 307	653.0, 24 094	652.6, 20 800
	Peak 4	—	655.6, 23 371	655.1, 18 093	654.3, 22 707
	Spin coupling	—	11.8	11.7	11.5
	Ratio Mn(IV) : Mn(III)	—	1.1	1.3	1.4
Mn 3s	Peak 1	83.12	83.18	83.55	83.36
	Peak 2	88.18	88.26	88.83	88.72
	Satellite	—	—	93.38	92.01
	Splitting	5.1	5.1	5.3	5.4
La 3d	Peak 1	834.19	834.52	833.9	834.0
	Peak 2	838.13	838.32	838.2	838.5
	Peak 3	836.46	836.79	836.0	836.2
	Peak 4	850.95	851.29	850.8	850.9
	Peak 5	854.91	855.26	855.1	855.3
	Peak 6	853.09	853.68	852.9	853.1
	La $3d_{5/2}$ splitting	3.9	3.8	4.3	4.4
	Spin coupling	16.8	16.8	16.9	16.8
O 1s	Peak 1	529.3, 4867	529.3, 26 741	529.3, 46 686	529.7, 37 254
	Peak 2	531.3, 6909	531.1, 51 708	531.5, 44 746	530.9, 28 693
	Peak 3	533.4, 1940	533.0, 16 494	534.0, 1472	532.2, 6739
	Peak 4	—	534.6, 6911	—	—

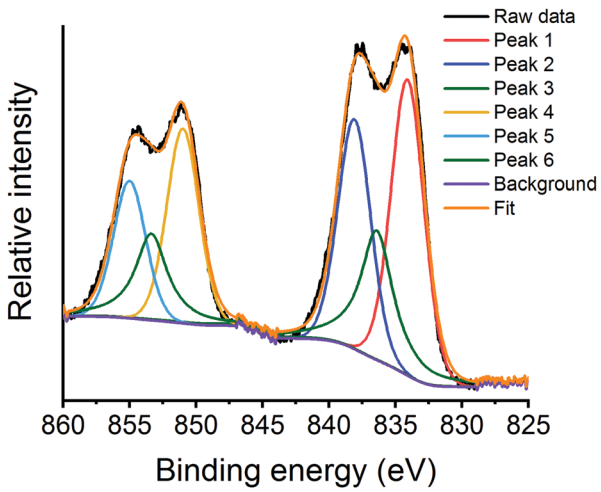

Fig. 12 La 3d XPS region for the argon milled catalyst showing the deconvoluted peaks at RT under a N_2O atmosphere.

the area of peak 1, arising due to lattice-type oxygens, is observed on exposure to N_2O. This could indicate a possible rearrangement of the surface structure due to N_2O interaction. On increasing the temperature to 400 °C the surface adsorbed species decrease. Further increase of the temperature to 600 °C shows a significant change in the peak shape, along with a 0.5 eV energy increase in the binding energy of peak 1. Here, the change in relative oxygen species abundance and peak positions could relate to either the hydrothermal removal of adsorbed oxygen species from the surface, as seen in the La 3d region (Table 2), or changes due to the Mn enivronment.[66,67] The Mn 2p and Mn 3s XPS data confirm that under these conditions the surface Mn species are relatively unchanged, whilst at greater depths oxygen is transferred towards the surface. Considering, that the O 1s data is acquired at the same depth penetration as the Mn 2p, it infers that the changes observed are correlated to changes in La speciation.

Both the air milled and sol–gel prepared $LaMnO_3$ also recorded a higher proportion of adsorbed species at the surface on exposure to N_2O (Tables S4 and S5) (Fig. S16 and S17) (ESI†). Significantly, the air milled and sol–gel catalysts do not have peak 4, fitted at 534.6 eV for the argon milled $LaMnO_3$, present within the O 1s region. This suggests that there are distinct surface sites for the argon milled $LaMnO_3$ that are involved in the deN_2O process at lower temperatures, increasing the catalytic activity (Fig. 10).[58,59] Furthermore, the air milled catalyst also suggests a rearrangement in surface structure due to exposure of N_2O, as a reduction in peak 1, corresponding to lattice-type oxygen, is observed.

The deN_2O catalytic testing observed an abrupt change to the light off profiles for the ball milled prepared samples that have been assigned to a phase transformation (Fig. 10). This behaviour mirrors what is found in the O 1s XPS data; between 400 °C and 600 °C there are significant changes within the O 1s profile for the balled milled samples. Conversely, the sol–gel prepared $LaMnO_3$ shows a similar peak profile within the O 1s region at both 400 °C and 600 °C, suggesting a relatively stable oxygen environment.

Although the role of Mn towards the catalytic activity is clearly important, in this work the Mn 2p region shows minimal changes during deN_2O.[63] However, there are significant changes, within the La 3d and O 1s regions that have provided additional value in understanding the catalytic activity of these $LaMnO_3$ systems. Furthermore, variations within the *in situ* deN_2O NAP-XPS regions compared to the *ex situ* XPS reported in Section 3.2 show the importance in tuning the incident beam in order to achieve equivalent data for each XPS region at the same penetration depth.

 This journal is © the Owner Societies 2020

Open Access Article. Published on 30 Qasa Dirri 2020. Downloaded on 22/04/2026 6:39:19 AM.
This article is licensed under a Creative Commons Attribution 3.0 Unported Licence.

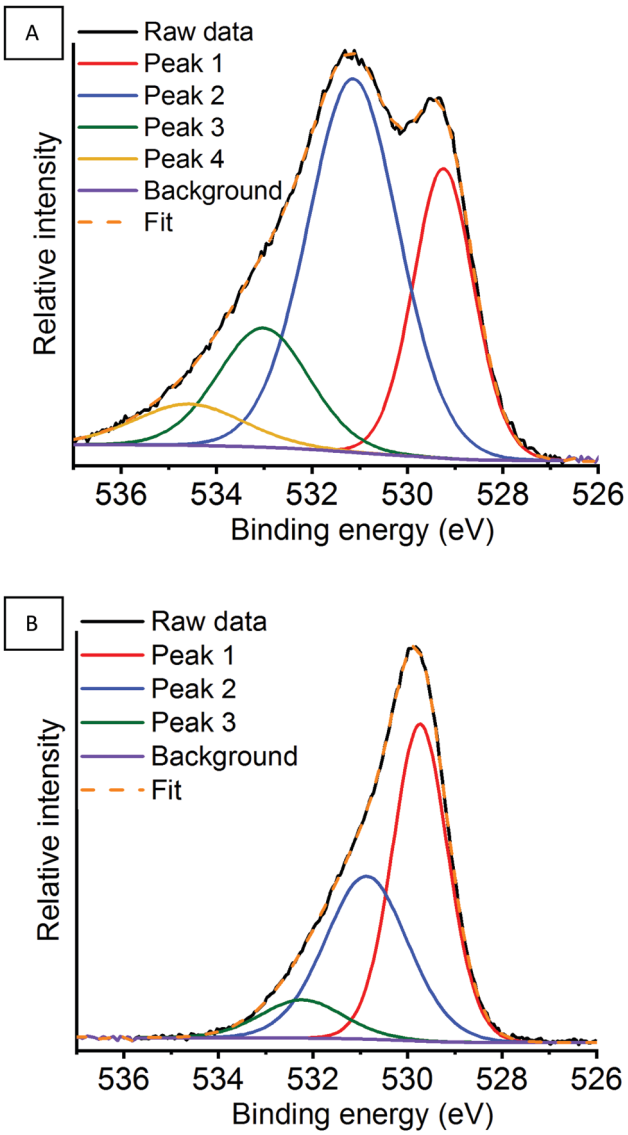

Fig. 13 O 1s region for the argon milled catalyst showing the deconvoluted peaks at (A) RT and (B) 600 °C under a N_2O atmosphere.

4. Conclusions

Here we have successfully provided in-depth insights into understanding the electronic and geometric changes during the mechanochemical synthesis of $LaMnO_3$. By performing *ex situ* HERFD measurements on 'time-slices' during milling we successfully identified the reduction of precursor Mn_2O_3 features within the pre-edge region and the evolution of peaks assigned to $LaMnO_3$. However, significant alterations are observed within the ball milled perovskite which indicate disruption to the Mn–La coordination, specifically to the lack of Mn 4p La 5d hybridisation, in comparison to the sol–gel prepared $LaMnO_3$. XES performed at the MnK$\beta_{1,3}$ emission line suggest a 'bulk' Mn(III) oxidation state throughout the mechanochemical synthesis.

Efforts to perform *in situ* milling and to replicate the conditions experienced during milling by *in situ* high pressure experiments on La_2O_3 and Mn_2O_3 precursors were unable to induce structural changes. This confirms that the mechanochemical synthesis of these metal oxide systems are extremely complicated to monitor *in situ*.

Investigating how the milling atmosphere effects the formation of the perovskite phase, shows that an argon environment decreases the proportion of crystalline $LaMnO_3$ after 4 h of milling, compared to an air milling atmosphere. However, performing deN_2O shows this argon milled catalyst to have an improved performance at lower temperatures compared to the air milled and sol–gel $LaMnO_3$. With the bulk structural analysis of the ball milled materials reporting similar structures it indicated that the catalytic activity of deN_2O is strongly correlated to the proportion of oxygen vacancies recorded at the surface from *ex situ* XPS.

By performing *in situ* NAP-XPS deN_2O we were able to further the understanding of this improved catalytic activity whilst studying the different $LaMnO_3$ catalysts under working conditions. Within the O 1s region the argon milled catalyst showed a higher proportion of adsorbed species on exposure to N_2O at RT, indicating an increase interaction with this species. It also highlighted that all catalysts remained with a mixed Mn(III)/Mn(IV) valency, even at elevated temperatures of 600 °C whilst working under catalytic conditions.

This work, therefore, demonstrates how the use of further advanced characterisation, such as HERFD, XES and NAP-XPS, can provide an in-depth understanding of the electronic, structural and surface properties of $LaMnO_3$ induced by the mechanochemical synthesis.

Conflicts of interest

There are no conflicts to declare.

Acknowledgements

The authors acknowledge Diamond Light Source for provision of beamtimes (experiments SP20129, SP20200 and SP22063) along with the UK Catalysis Hub for provision of beamtime SP15151-8. The staff on B18, I20-Scanning, I20-EDE and B07-C at Diamond Light Source are thanked. Particularly Dr Diego Gianolio is thanked for his assistance in collecting data on B18 and Dave Grinter, Pilar Ferrer-Escorihuela and Rosa Arrigo for establishing the B07-C beamline. Also, to the ID15A beamline and their staff at the European Synchrotron Radiation Facility and particularly to the Ruđer Bošković Institute for the use of their *in situ* milling set-up (experiment CH-5331). The RCaH are acknowledged for use of facilities and staff support. Johnson Matthey is acknowledged for their provision of precursor materials and milling equipment. The Johnson Matthey advanced analytical department are also thanked for their help and support throughout the project. The UK Catalysis Hub is kindly thanked for resources and support provided *via* our membership of the UK Catalysis Hub Consortium (portfolio grants EP//K014706/1, EP/K014668/1, EP/K014854/1, EP/K014714/1 and EP/I019693/1). The University of Southampton and EPSRC are thanked for the iCASE studentship of RHB. PW and KM wish to acknowledge the

STFC for funding the position of KM (ST/R002754/1). PW and MC wish to acknowledge the EPSRC for funding the position of MC (EP/R011710/1). All data supporting this study are openly available from the University of Southampton repository at DOI: 10.5258/SOTON/D1342.

Open Access Article. Published on 30 Qasa Dirri 2020. Downloaded on 22/04/2026 6:39:19 AM. This article is licensed under a Creative Commons Attribution 3.0 Unported Licence.

References

1 J. F. Jenck, F. Agterberg and M. J. Droescher, *Green Chem.*, 2004, **6**, 544.
2 D. C. Koningsberger, B. L. Mojet, G. E. Van Dorssen and D. E. Ramaker, *Top. Catal.*, 2000, **10**, 143–155.
3 M. Newville, Fundamentals of XAFS, 2004.
4 J. Evans, *X-Ray Absorption Spectroscopy for the Chemical and Materials Sciences*, John Wiley & Sons Ltd, 2017.
5 R. H. Blackmore, M. E. Rivas and T. E. Erden, *Dalton Trans.*, 2020, **49**, 232–240.
6 S. Lafuerza, J. García, G. Subías, J. Blasco and P. Glatzel, *Phys. Rev. B*, 2016, **93**, 31–33.
7 F. De Groot, G. Vankó and P. Glatzel, *J. Phys.: Condens. Matter*, 2009, **21**, 104207.
8 P. Glatzel and U. Bergmann, *Coord. Chem. Rev.*, 2005, **249**, 65–95.
9 P. Glatzel, T. C. Weng, K. Kvashnina, J. Swarbrick, M. Sikora, E. Gallo, N. Smolentsev and R. A. Mori, *J. Electron Spectrosc. Relat. Phenom.*, 2013, **188**, 17–25.
10 S. Hayama, G. Duller, J. P. Sutter, M. Amboage, R. Boada, A. Freeman, L. Keenan, B. Nutter, L. Cahill, P. Leicester, B. Kemp, N. Rubies and S. Diaz-Moreno, *J. Synchrotron Radiat.*, 2018, **25**, 1556–1564.
11 S. Limandri, S. Ceppi, G. Tirao, G. Stutz, C. G. Sánchez and J. A. Riveros, *Chem. Phys.*, 2010, **367**, 93–98.
12 T. A. Tyson, Q. Qian, C.-C. Kao, J.-P. Rueff, F. M. F. De Groot, M. Croft, S.-W. Cheong, M. Greenblatt and M. A. Subramanian, *Phys. Rev. B: Condens. Matter Mater. Phys.*, 1999, **60**, 4665–4674.
13 I. Halasz, S. A. J. Kimber, P. J. Beldon, A. M. Belenguer, F. Adams, V. Honkimäki, R. C. Nightingale, R. E. Dinnebier and T. Friščić, *Nat. Protoc.*, 2013, **8**, 1718–1729.
14 T. Frišči, I. Halasz, P. J. Beldon and A. M. Belenguer, *Nat. Chem.*, 2012, **5**, 66–73.
15 H. K. Mao, J. Xu and P. M. Bell, *J. Geophys. Res.*, 1986, **91**, 4673.
16 X. Hong, M. Newville, V. B. Prakapenka, M. L. Rivers and S. R. Sutton, *Rev. Sci. Instrum.*, 2009, **80**, 073908.
17 M. Newville, *J. Synchrotron Radiat.*, 2001, **8**, 322–324.
18 B. Ravel and M. Newville, *J. Synchrotron Radiat.*, 2005, **12**, 537–541.
19 M. C. Biesinger, B. P. Payne, A. P. Grosvenor, L. W. M. Lau, A. R. Gerson and R. S. C. Smart, *Appl. Surf. Sci.*, 2011, **257**, 2717–2730.
20 M. Bauer, *Phys. Chem. Chem. Phys.*, 2014, **16**, 13827–13837.
21 D. Rybicki, M. Sikora, J. Przewoznik, C. Kapusta and J. F. Mitchell, *Phys. Rev. B*, 2018, **97**, 1–8.
22 F. Farges, *Phys. Rev. B: Condens. Matter Mater. Phys.*, 2005, **71**, 1–14.
23 D. C. Radu, P. Glatzel, W. M. Heijboer, J. H. Bitter, B. M. Weckhuysen and F. M. F. de Groot, *Mn and Fe Ions and Oxo clusters in ZSM-5: Pushing the limits of X-ray Spectroscopy*, Elsevier B.V., 2007, vol. 170.
24 L. A. Isupova, G. M. Alikina, S. V. Tsybulya, A. N. Salanov, N. N. Boldyreva, E. S. Rusina, I. A. Ovsyannikova, V. A. Rogov, R. V. Bunina and V. A. Sadykov, *Catal. Today*, 2002, **75**, 305–315.
25 V. Cuartero, S. Lafuerza, M. Rovezzi, J. García, J. Blasco, G. Subías and E. Jiménez, *Phys. Rev. B*, 2016, **94**, 1–10.
26 A. Y. Ignatov, N. Ali and S. Khalid, *Phys. Rev. B: Condens. Matter Mater. Phys.*, 2001, **64**, 1–16.
27 F. M. F. De Groot, S. Huotari, R. J. Cava, T. Lorenz and M. Reuther, 2008, arXiv:0802.2744.
28 R. Baran, L. Valentin, J. M. Krafft, T. Grzybek, P. Glatzel and S. Dzwigaj, *Phys. Chem. Chem. Phys.*, 2017, **19**, 13553–13561.
29 S. D. Gamblin and D. S. Urch, *J. Electron Spectrosc. Relat. Phenom.*, 2001, **113**, 179–192.
30 M. A. Beckwith, M. Roemelt, C. Duboc, T. Weng, U. Bergmann, P. Glatzel, F. Neese and S. Debeer, *Inorg. Chem.*, 2011, 8397–8409.
31 S. L. James, C. J. Adams, C. Bolm, D. Braga, P. Collier, T. Friščić, F. Grepioni, K. D. M. Harris, G. Hyett, W. Jones, A. Krebs, J. Mack, L. Maini, A. G. Orpen, I. P. Parkin, W. C. Shearouse, J. W. Steed and D. C. Waddell, *Chem. Soc. Rev.*, 2012, **41**, 413–447.
32 P. Baláž, M. Achimovičová and M. Baláž, *Chem. Soc. Rev.*, 2013, **42**, 7571–7637.
33 M. a Pena and J. L. G. Fierro, *Chem. Rev.*, 2001, **101**, 1981–2017.
34 P. Granger, V. I. Parvulescu, S. Kaliaguine and W. Prellier, *Perovskites and Related Mixed Oxides Concepts and Applications*, Wiley-VCH, 2015.
35 Y. Syono and S. Akimoto, *J. Phys. Soc. Jpn.*, 1969, **26**, 993–999.
36 J. A. M. Van Roosmalen, P. van Vlaanderen and E. H. P. Cordfunke, *J. Solid State Chem.*, 1995, **114**, 516–523.
37 Y. Zhao, *Materials*, 2012, **5**, 1413–1438.
38 L. B. Mccusker, R. B. Von Dreele, D. E. Cox, D. Louër and P. Scardi, *J. Appl. Crystallogr.*, 1999, **32**, 36–50.
39 K. Jirátová, J. Mikulová, J. Klempa, T. Grygar, Z. Bastl and F. Kovanda, *Appl. Catal., A*, 2009, **361**, 106–116.
40 V. P. Santos, M. F. R. Pereira, J. J. M. Órfão and J. L. Figueiredo, *Appl. Catal., B*, 2010, **99**, 353–363.
41 A. Machocki, T. Ioannides, B. Stasinska, W. Gac, G. Avgouropoulos, D. Delimaris, W. Grzegorczyk and S. Pasieczna, *J. Catal.*, 2004, **227**, 282–296.
42 S. K. Gupta, M. Sahu, P. S. Ghosh, D. Tyagi, M. K. Saxena and R. M. Kadam, *Dalton Trans.*, 2015, **44**, 18957–18969.
43 Y. Yang, S. Zhang, S. Wang, K. Zhang, H. Wang, J. Huang, S. Deng, B. Wang, Y. Wang and G. Yu, *Environ. Sci. Technol.*, 2015, **49**, 4473–4480.
44 J. Zhu, H. Li, L. Zhong, P. Xiao, X. Xu, X. Yang, Z. Zhao and J. Li, *ACS Catal.*, 2014, **4**, 2917–2940.
45 N. Gunasekaran, S. Rajadurai and J. J. Carberry, *Catal. Lett.*, 1995, **35**, 373–382.
46 N. Russo, D. Mescia, D. Fino, G. Saracco and V. Specchia, *Ind. Eng. Chem. Res.*, 2007, **46**, 4226–4231.
47 H. Najjar and H. Batis, *Catal. Rev.*, 2016, **58**, 371–438.
48 C. Escudero, P. Jiang, E. Pach, F. Borondics, M. W. West, A. Tuxen, M. Chintapalli, S. Carenco, J. Guo and M. Salmeron, *J. Synchrotron Radiat.*, 2013, **20**, 504–508.
49 N. H. Turner, *Anal. Chem.*, 1986, **58**, 153–165.
50 S. Jaiswar and K. D. Mandal, *J. Phys. Chem. C*, 2017, **121**, 19586–19601.

Open Access Article. Published on 30 Qasa Dirri 2020. Downloaded on 22/04/2026 6:39:19 AM.
This article is licensed under a Creative Commons Attribution 3.0 Unported Licence.

51 A. J. Nelson, J. G. Reynolds and J. W. Roos, *J. Vac. Sci. Technol., A*, 2000, **18**, 1072–1076.
52 M. A. Stranick, *Surf. Sci. Spectra*, 1999, **6**, 31–38.
53 M. A. Stranick, *Surf. Sci. Spectra*, 1999, **6**, 39–46.
54 D. J. Lam, B. W. Veal and D. E. Ellis, *Phys. Rev. B: Condens. Matter Mater. Phys.*, 1980, **22**, 5730–5739.
55 V. R. Galakhov, M. Demeter, S. Bartkowski, M. Neumann, N. A. Ovechkina, E. Z. Kurmaev, N. I. Lobachevskaya, Y. M. Mukovskii, J. Mitchell and D. L. Ederer, *Phys. Rev. B: Condens. Matter Mater. Phys.*, 2002, **65**, 1–4.
56 A. Staykov, H. Téllez, T. Akbay, J. Druce, T. Ishihara and J. Kilner, *Chem. Mater.*, 2015, **27**, 8273–8281.
57 H. Najjar, J. F. Lamonier, O. Mentré, J. M. Giraudon and H. Batis, *Appl. Catal., B*, 2011, **106**, 149–159.
58 T. A. Egerton, F. S. Stone and J. C. Vickerman, *J. Catal.*, 1974, **33**, 307–315.
59 F. Kapteijn, J. Rodriguez-Mirasol and J. A. Moulijn, *Appl. Catal., B*, 1996, **9**, 25–64.
60 R. Dudric, A. Vladescu, V. Rednic, M. Neumann, I. G. Deac and R. Tetean, *J. Mol. Struct.*, 2014, **1073**, 66–77.
61 T. S. Kharlamova, A. S. Matveev, A. V. Ishchenko, A. N. Salanov, S. V. Koshcheev, A. I. Boronin and V. A. Sadykov, *Kinet. Catal.*, 2014, **55**, 361–371.
62 D. F. Mullica, C. K. C. Lok, H. O. Perkins and V. Young, *Phys. Rev. B: Condens. Matter Mater. Phys.*, 1985, **31**, 4039–4042.
63 M. F. Sunding, K. Hadidi, S. Diplas, O. M. Løvvik, T. E. Norby and A. E. Gunnæs, *J. Electron Spectrosc. Relat. Phenom.*, 2011, **184**, 399–409.
64 Y. Zhang-Steenwinkel, J. Beckers and A. Bliek, *Appl. Catal., A*, 2002, **235**, 79–92.
65 M. E. Rivas, C. E. Hori, J. L. G. Fierro, M. R. Goldwasser and A. Griboval-Constant, *J. Power Sources*, 2008, **184**, 265–275.
66 J. G. Kang, Y. Il Kim, D. Won Cho and Y. Sohn, *Mater. Sci. Semicond. Process.*, 2015, **40**, 737–743.
67 P. Fleming, R. A. Farrell, J. D. Holmes and M. A. Morris, *J. Am. Ceram. Soc.*, 2010, **93**, 1187–1194.